Conwell, C.T., et al., 2022, Nd isotopic evidence for enhanced mafic weathering leading to Ordovician cooling: Geology, v. 50, https://doi.org/10.1130/G49860.1

Supplementary Materials for

# Nd isotopic evidence for enhanced mafic weathering leading to Ordovician cooling

Christopher T. Conwell*, Matthew R. Saltzman, Cole T. Edwards, Elizabeth M. Griffith, Y. Datu Adiatma

*Corresponding author. Email: conwell.30@osu.edu

**This PDF file includes:**

Supplementary Text
Figs. S1 to S10
Supplementary References

**Other Supplementary Materials for this manuscript include the following:**

Data S1 (Isotope measurements)
Data S2 (Model outputs)

# Supplementary Text

## 1. Materials and Methods

### *Sampling*

The section measured in the Antelope Range of central Nevada outcrops on the south side of Hill 8308 in the USGS Ninemile Peak quadrangle [39.15597° N, 116.0257° W] (Fig. S6). Hill 8308 is marked by two north-south running gullies. The base of the section begins ~150 m east of the eastern gully where most of the section is exposed and is marked with two stripes of orange paint on an outcrop bordering the Jeep trail. Where possible, an orange stripe was painted every 6 m and the meterage written on the rock with a marker pen. Sample collection required traversing along strike between small outcrops, especially for the first ~40 m of the Antelope Valley Limestone and all of the Copenhagen Formation. Member A of the Copenhagen Formation, a resistant sandstone layer, appeared to be faulted across the gully. We measured to the base of Copenhagen Member A on the west side of the gully which had more frequent outcrops. Outcrop above Copenhagen Member A was sparse and in some cases sampling required removal of several inches of overlying soil. Outcrop was entirely covered for several tens of meters below the resistant Eureka Quartzite.

### *Stratigraphic age model*

Conodont biostratigraphy of the stratigraphic units measured here was characterized by Ethington (1969), Harris et al. (1979), Spencer (1984), and Sweet et al. (2005). The Hill 8308 conodont biostratigraphic framework is summarized in Saltzman et al. (2014) and is the age model used here. Carbonate strata at Hill 8308 contain conodonts of both the North American Midcontinent and North Atlantic provincial faunas. Key index fossils in the upper Antelope Valley Limestone include *Histiodella holodentata*, *Cahabagnathus friendsvillensis*, and *Pygodus serra* (Fig. S7A). In Members B and C of the Copenhagen Formation (overlying the Member A sandstone) occur *C. sweeti*, *P. anserinus*, *Phragmodus undatus*, *Baltoniodus gerdae*, and *Plectondina tenuis* (Fig. S7A). This biostratigraphic framework is the basis for age-depth models of previous datasets from this section (Saltzman and Young, 2005; Young et al., 2009; Saltzman et al., 2014; Edwards et al., 2021)

To facilitate comparison of our dataset with other seawater proxy records reported from the same section, we build our age model using sample ages reported for this section in Saltzman et al. (2014) and Edwards et al. (2021) as age tie points (i.e., age-dated stratigraphic horizons) (Fig. S7B). Sample ages from Saltzman et al. (2014) are recalibrated relative to Ordovician stage boundaries in the 2020 Geologic Timescale (Goldman et al., 2020). We linearly interpret accommodation rate between sample tie points and extrapolate the age-depth gradient below the lowest tie point (Fig. S7B).

### *Chemical preparation and analysis*

Carbonate rocks were prepared for Nd isotopic analysis following the methods of Fanton et al. (2002). ~2 g of carbonate rock was collected per sample. Visibly altered surfaces were removed using a handheld rotary tool. Localized carbonate alteration (spheres or stringers of red–orange mineralization) could not be avoided in all samples but are not expected to affect $\varepsilon_{Nd(t)}$ (Banner et al., 1988). Samples were powdered by ceramic mortar and pestle and dissolved in distilled TraceMetal-grade 6N HCl following conventional methods for bulk carbonate

analysis (Holmden et al., 1998; Fanton et al., 2002; Theiling et al., 2017). We use a stronger acid for sample digestion for Nd analysis than for Sr analysis to efficiently leach larger volumes of rock powder, making the assumption that the isotopic composition of Nd leached from the insoluble phase is not differentiated from the acid-soluble phase (Fanton et al., 2002). Sample solutions were passed through 13 mm 0.22 mm Luer-Lock syringe filters to remove fine particulates and mixed with a $^{150}Nd$–$^{147}Sm$ spike in a ~1:10 spike:sample ratio. Before spiking, an aliquot of the sample solution was separated for concentration measurement on a Perkin Elmer Elan 6000 quadrupole ICP-MS in the School of Earth Sciences at Ohio State (PI J. Olesik). REEs were separated from the bulk sample solution by BioRad AG50-X8 cation exchange resin in 6 mL quartz glass columns. To isolate Nd and Sm, the REE fraction was passed through HDEHP-coated Teflon powder resin in 4.5 mL quartz glass columns, where separate Sm and Nd fractions were collected. For details on column chromatography procedure, refer to Foland and Allen (1991). $^{143}Nd/^{144}Nd$ measurements are corrected for spike contribution, and sample $^{147}Sm/^{144}Nd$ is used to correct for contribution of post-depositional radiogenic $^{143}Nd$ by in-situ $^{147}Sm$ decay (DePaolo and Wasserburg, 1976).

Bulk rock $^{87}Sr/^{86}Sr$ measurements were made to supplement $^{87}Sr/^{86}Sr$ measurements of conodont apatite from Saltzman et al. (2014). For a subset of the same carbonate samples analyzed for $\varepsilon_{Nd(t)}$, hand samples were cut and polished with a diamond-grit hand polisher to reveal areas of pristine micrite. ~200 mg powder was drilled from each sample, giving preference to areas free of skeletal material or alteration, though in some samples such areas could not be avoided. Following methods of Edwards et al. (2015) and references therein, ~60 mg of powder was weighed by microbalance, cleaned with three rinses of TraceMetal-grade 1M ammonium acetate, and dissolved in TraceMetal-grade 4% acetic acid. A weaker acid is used for digestion for Sr analysis than for Nd analysis to avoid releasing contaminant Sr from the insoluble phase (Montañez et al., 1996; Edwards et al., 2015). An aliquot of the sample solution was separated for concentration measurement using a Perkin Elmer Optima 4300 DV ICP-OES in the School of Earth Sciences at Ohio State (PI J. Olesik). Sr was isolated from the sample solution using two passes through BioRad AG50-X8 cation exchange resin in 6 mL quartz glass columns.

All $^{143}Nd/^{144}Nd$, $^{147}Sm/^{152}Sm$, and $^{87}Sr/^{86}Sr$ ratios were measured by a ThermoFisher Triton Plus Thermal Ionization Mass Spectrometer (TIMS) in the School of Earth Sciences at Ohio State (PI E.M. Griffith). Sm (~100 ng/sample) and Nd (~500 ng/sample) were loaded on outgassed Re double filaments with $H_3PO_4$, whereas Sr (~1 mg/sample) was loaded on outgassed single Re filaments with a $Ta_2O_5$ activator. $^{143}Nd/^{144}Nd$ was measured at a signal intensity of 4V in 9 blocks of 20 cycles; $^{147}Sm/^{152}Sm$ at a signal intensity of 0.2 V for 3 blocks of 20 cycles; $^{87}Sr/^{86}Sr$ at a signal intensity of 4V for 10 blocks of 20 cycles each. For all elements, a defocus baseline reading was taken between blocks. For $^{143}Nd/^{144}Nd$ and $^{147}Sm/^{152}Sm$, each individual cycle has one integration of 8.389 seconds with a 5.000 second dwell time; for $^{87}Sr/^{86}Sr$, one integration of 16.777 seconds with a 3.000 second dwell time. All ratios were measured in a static method with virtual amplifier rotation. Ratios were normalized following the method of Foland and Allen (1991), where each is applied with an exponential law: for $^{143}Nd/^{144}Nd$, ratios normalized to $^{146}Nd/^{144}Nd = 0.7219$; for $^{147}Sm/^{152}Sm$, ratios normalized to $^{149}Sm/^{152}Sm = 0.516858$; for $^{87}Sr/^{86}Sr$, ratios normalized to $^{88}Sr/^{86}Sr = 8.375209$. Average La Jolla standard measurement is $^{143}Nd/^{144}Nd = 0.5118503 \pm 9x10^{-6}$ (n = 13; 1σ error) with a median internal error (mean absolute error) of $1.75x10^{-6}$. Average SRM-987 value is $^{87}Sr/^{86}Sr = 0.710260 \pm 4x10^{-6}$ (n=3; 1σ error) with a median internal error (mean absolute error) of $2.97x10^{-6}$. For each

"wheel" of samples loaded in the TIMS, at least two filaments loaded with standard were included. Standard analyses bracket every 5–6 sample analyses.

## 2. Sedimentary provenance and correlation

### *Isotopic proxy signals and the deposition of Copenhagen Formation Member A*

As discussed in the main text, the change in $^{87}Sr/^{86}Sr$, $\varepsilon_{Nd(t)}$, and $\delta^{18}O$ proxy records is coincident with a change in lithology from relatively pure carbonates of the Antelope Valley Limestone to the thin (~9 m), quartzitic sandstone of Member A of the Copenhagen Formation (Ross, 1976). This sandstone is interpreted to be regionally correlative with the base of the thicker Eureka Quartzite that outcrops throughout the Great Basin (Ross, 1976). The Eureka Quartzite is highly diachronous, however, and correlating the base of unit to widely deposited sandstones outside the Great Basin remains challenging (Ross, 1976). Correlation of regional sandstone units within a broader first–order sequence stratigraphic framework could reveal the influence of fluctuating sea level on weathering proxy signals, as suggested by other work (Fanton et al., 2002).

## 3. Fidelity and timing of isotopic signals

### *$^{87}Sr/^{86}Sr$ signal*

Previous bulk carbonate and conodont apatite $^{87}Sr/^{86}Sr$ measurements from this location (Young et al., 2009; Edwards et al., 2015) align well with the Laurentian conodont apatite $^{87}Sr/^{86}Sr$ composite curve (Saltzman et al., 2014), indicating that both sample media from this section record primary seawater $^{87}Sr/^{86}Sr$ values.

### *$\varepsilon_{Nd(t)}$ signal*

$\varepsilon_{Nd(t)}$ measurements presented here are the first from this section, but studies of other early Paleozoic carbonate successions show that carbonate rocks are a reliable archive for seawater $\varepsilon_{Nd(t)}$ (Holmden et al., 1998; Fanton et al., 2002; Theiling et al., 2017). Although the observed changes in $\varepsilon_{Nd(t)}$ suggest an increase in mafic weathering, we must also consider the influence of intermediate–felsic crustal weathering or mixing with Iapetus Ocean water to evaluate the role of mafic weathering in Middle–Late Ordovician $CO_2$ drawdown. Studies of shale $\varepsilon_{Nd(t)}$ (Andersen and Samson, 1995; Swanson-Hysell and Macdonald, 2017) and detrital zircon age populations (Gehrels and Pecha, 2014; Karabinos et al., 2017) suggest a widespread Laurentian increase in weathering of dominantly intermediate–felsic Grenville crust (~1.0–1.2 Ga; $\varepsilon_{Nd(t)} = \sim -6$; Andersen and Samson, 1995) during the Taconic orogeny. If the seawater $\varepsilon_{Nd(t)}$ signal is largely the product of intermediate–felsic Grenville weathering, this would reduce the amount of atmospheric $CO_2$ drawdown and cooling. Additionally, upwelling of high-$\varepsilon_{Nd(t)}$ waters from the eastern Iapetus ocean ($\varepsilon_{Nd(t)} = -5$ to $-9$; Keto and Jacobsen, 1987) could produce a positive shift in seawater $\varepsilon_{Nd(t)}$. However, enrichment of detrital chromite (Hiscott, 1984) and bulk rock Cr (Garver et al., 1996) in shales of the eastern Taconic foreland (northern Appalachians in modern coordinates) requires weathering of a mafic source rock, and $^{87}Sr/^{86}Sr$ of Grenville crust is too radiogenic to produce the observed trend (>0.710 at 460 ma from initial Archean values of ~0.704; Krogh and Hurley, 1968). Additionally, the occurrence of Ordovician

mafic and ultramafic bodies spanning the Taconic margin, and in some cases well-preserved ophiolite sequences, indicate that mafic rocks were a substantial component of the Middle–Late Ordovician Taconic margin (Hatcher, 2010). Alignment of carbonate $\varepsilon_{Nd(t)}$ with shale $\varepsilon_{Nd(t)}$ measurements suggest that the seawater $\varepsilon_{Nd(t)}$ shift was imparted from a change in weathering source lithology rather than eastern Iapetus seawater. Thus, weathering of mafic rocks likely played a major role in driving the large shift in seawater $\varepsilon_{Nd(t)}$.

Comparison of acid leaching methods for digestion of carbonate sediments for $\varepsilon_{Nd(t)}$ analysis demonstrates that overly strong leaching methods can liberate Nd from detrital phases with implications for the $\varepsilon_{Nd(t)}$ composition of the acid-soluble phase (Abbott et al., 2016, 2021). This has also been demonstrated in Ordovician carbonates, where Fanton et al. (2002) found a positive correlation between wt% insoluble residue (generally <20–30%) and Nd concentration using our same leaching method (6 M HCl). However, Fanton et al. (2002) also found that conodont apatite records the same $\varepsilon_{Nd(t)}$ as the acid-soluble phase of the carbonate host rock, and interpret that the mobile Nd reservoir in the insoluble phase has $\varepsilon_{Nd(t)}$ identical to that of the acid-soluble phase. This contrasts with a compilation of $\varepsilon_{Nd(t)}$ measurements of primarily pelagic sediments that demonstrates covariance between detrital and authigenic phases, suggesting a primary detrital influence on $\varepsilon_{Nd(t)}$ of both authigenic Fe-Mn phases and bioapatite deposited in detrital-rich sediments (Abbott et al., 2021). We note that the carbonate content of these pelagic deposits (generally <30 wt% carbonate) is less than is typical for Ordovician carbonates (generally >70–80 wt% carbonate; Fanton et al., 2002), therefore we would expect less of an influence from leaching of detrital sediments in our samples than has been demonstrated in pelagic sediments.

We cannot rule out that our carbonate $\varepsilon_{Nd(t)}$ signal is dominated by Nd contribution from the detrital (insoluble) phase, thereby obscuring the seawater signal. However, regardless of whether the shift to juvenile $\varepsilon_{Nd(t)}$ in the acid-soluble portion of our carbonate samples reflects a change in seawater composition or the appearance of juvenile clastic sediments following the arrival of more argillaceous Copenhagen Formation carbonates, our samples still resolve this shift in an age framework that allows for direct comparison to seawater $^{87}Sr/^{86}Sr$ and $\delta^{18}O$ proxy signals. Additionally, this shift to juvenile values has been observed in other carbonate sections at horizons that do not show a shift to more argillaceous lithology (Fanton et al., 2002).

### *$\delta^{18}O$ signal*

Well-preserved conodonts in the Antelope Range section (Conodont Alteration Index of 1–2) are unlike the thermally altered conodonts found elsewhere in the Great Basin or the Taconic foreland and have produced $\delta^{18}O$ values that fit well within a global compilation (Edwards et al., 2021; Fig. 1C) suggesting preservation of a primary seawater signal. We consider the $\delta^{18}O$ signal recorded in the Antelope Range to reflect cooling in the tropics related to global cooling for several reasons. Foremost, these measurements align well with globally compiled SIMS and TC/EA measurements of conodont $\delta^{18}O$. Local influence from changes in ocean circulation due to regional tectonics is unlikely because this location in Nevada represents a passive margin. Paleolatitudinal constraints place Laurentia at tropical latitudes for the whole Ordovician, ruling out paleogeographic influence (Swanson-Hysell and Macdonald, 2017). Previous work suggests that an increased latitudinal temperature gradient and rising sea levels could have increased upwelling of cool bottom waters (Rasmussen et al., 2016), consistent with cherty and phosphatic deposition (Pope and Steffen, 2003). However, there is no reason to expect that upwelling would have only affected the carbonate platform covering modern central Nevada, and not the other

carbonate platforms holding conodonts whose values make up the existing $\delta^{18}O$ record. Regardless, an increase in upwelling of cold bottom waters is consistent with global cooling, though it could mean that the $\delta^{18}O$ record in central Nevada overestimates the amount of cooling experienced globally.

The LOESS smoothing curve of $\delta^{18}O$ measurements from our section (Fig. 2C) suggests an inflection at ~461 Ma to higher cooler values. However, we emphasize that $\delta^{18}O$ data through this interval of change in weathering proxy signals (~463–458) are too sparse to confidently place the timing of an inflection. It is possible that cooling began prior to the supposed inflection 461 Ma (but following the shift in weathering proxies at 463 Ma), and that the three $\delta^{18}O$ measurements at ~461 Ma, representing samples from a single bed, record anomalously low $\delta^{18}O$ values similar to the two data points from the bed at ~458 Ma. However, it is also possible that this apparent ~2 Myr lag is a true signal which may be the result of a host of regional feedbacks such as oxidation of buried organic material during Taconic uplift, reduced upwelling of cold bottom waters during terrane accretion or other changes in vertical or lateral water mass mixing, or albedo feedbacks due to the presence of new landmass. Future investigations that increase data resolution through this interval and pair $\delta^{18}O$ with other paleoenvironmental proxies will be useful to test these hypotheses.

## 4. Carbon and $^{87}Sr/^{86}Sr$ mass balance modeling

### *Model results, silicate weathering sensitivity, and discussion*

Using the initial conditions of the original model, this updated degassing parameter causes a 17% decrease in global degassing during the modeled interval spanning 486 to 443 Ma (Fig. 3A). A 25% increase in weatherability which occurs at 463 Ma, consistent with the timing of increased juvenile weathering observed in $^{87}Sr/^{86}Sr$ and $\varepsilon_{Nd(t)}$ datasets, is required to produce the observed trend in $^{87}Sr/^{86}Sr$ measurements (Fig. 3B). In response to increased weatherability, the silicate weathering sink flux increases by 11% (Data S2; Fig. 3A).

To illustrate the importance of the silicate weathering sink, we tested a model scenario with constant weatherability and found that, although decreased degassing alone lowered $pCO_2$ by ~40%, the seawater $^{87}Sr/^{86}Sr$ record was not reproduced (Fig. S3). A separate model scenario with constant degassing also produced a satisfactory decrease in $pCO_2$ (~50%), but does not agree with subduction zone length- and zircon-based predictions of fluctuations in Ordovician degassing (McKenzie et al., 2016; Marcilly et al., 2021) (Fig. S4). Outputs for all model parameters are shown in Fig. S5. Our $pCO_2$ model result crosses the 12 PAL (3,360 ppmv) threshold required for widespread Ordovician ice sheet growth (Pohl et al., 2016) roughly coeval with shifts in proxy signals and deposition of the basal Copenhagen sandstone, supporting the possibility of a glacioeustatic influence (Fig. 3A).

### *Volcanic degassing flux derivation, limitations, and model sensitivity*

We tested several Ordovician reconstructions of relative volcanic arc activity to estimate global volcanic degassing rate through time (Fig. S8). Relative arc activity is based on arc-generated zircon age frequency through time (McKenzie et al., 2014, 2016; Torsvik et al., 2021; Cocks and Torsvik, in press) and is reported as a unitless parameter normalized to modern day arc activity (e.g., 1.5 times modern). Limitations to zircon-based degassing estimates include,

foremost, geographical and temporal sampling biases of zircon populations that require a correction of data "backfilling", or interpolation of zircon occurrences based on geological evidence (see supplementary material of McKenzie et al. (2016) for detailed discussion). Additionally, the conversion of relative zircon abundance to a volcanic degassing carbon flux is poorly constrained.

We assume that arc activity scales linearly with degassing rate, e.g. that 1.5 times modern arc activity equates to 1.5 times modern degassing. Therefore, we multiply the modern degassing rate used in the global carbon cycle model GEOCARBSULF (7.92 x $10^{12}$ mols C/yr; Berner (2006)) by the relative arc activity scaling factor of Torsvik et al. (2021; see also Marcilly et al., 2021; Cocks and Torsvik, in press) to compute degassing rate during the Ordovician. Applying this scaling of arc activity to modern degassing values gives degassing values that are too high to be balanced by our given silicate weathering rate (Fig. S8). One explanation for this is that the Ordovician predates the rise of pelagic calcifying organisms and is characterized by widespread carbonate deposition on continental shelves, therefore carbonate sediments were less likely to be recycled during subduction (Berner, 1991, 2006). We scale our degassing parameter by 0.44 so the initial condition of the degassing flux matches that of the original model in Young et al. (2009) (6 x $10^{12}$ mol C/yr), thereby balancing the initial condition of the silicate weathering flux (Fig. 3A). This highlights the non-uniqueness of our model. Although our model may not accurately predict absolute rates of degassing during the Ordovician, it reproduces $pCO_2$ trends within the constraints of $^{87}Sr/^{86}Sr$ and $\delta^{18}O$ measurements, tectonic activity reconstructions (Merdith et al., 2021; Cocks and Torsvik, in press), and published carbon cycle models (Berner, 2006; Lenton et al., 2018). A volcanic degassing sensitivity experiment shows the response of the silicate weathering feedback to different degassing scenarios (Fig. S9).

***Modeled $pCO_2$ to temperature***

To demonstrate one possible reconstruction of Ordovician paleotemperature (Fig. S10), we convert our $pCO_2$ model output to temperature using the temperature sensitivity to $pCO_2$ equation of GEOCARB models (Berner, 1994; Berner and Kothavala, 2001). This equation is also used in the latest version of COPSE (Lenton et al., 2018) where it is presented as:

$$\Delta T = (k_c * \ln(RCO_2)) - (k_l * t/570)$$

where $RCO_2$ is atmospheric $pCO_2$ normalized to present day concentration (280 ppm after Lenton et al. (2018)), $k_c$ is a temperature sensitivity to $pCO_2$ coefficient [°C], $k_l$ = 7.4 [°C] is a sensitivity coefficient to solar luminosity, and t = time [Myr ago] (Lenton et al., 2018). Using $k_c$ = 4.328 °C following the method of Lenton et al. (2018), which corresponds to a 3 °C temperature increase for a doubling of $pCO_2$, yielded paleotemperatures that were significantly lower than Ordovician $\delta^{18}O$ paleotemperature reconstructions (Grossman and Joachimski, 2020; Goldberg et al., 2021). We instead use $k_c$ = 7.646, corresponding to a 5.3 °C increase for a doubling of $CO_2$, which yields a temperature reconstruction in better agreement with $\delta^{18}O$ paleotemperature reconstructions (Fig. S10). This parametrization agrees with estimates of modern climate sensitivity that suggest as high as a 4.5–5.6 °C increase per doubling of $CO_2$ (Zelinka et al., 2020).

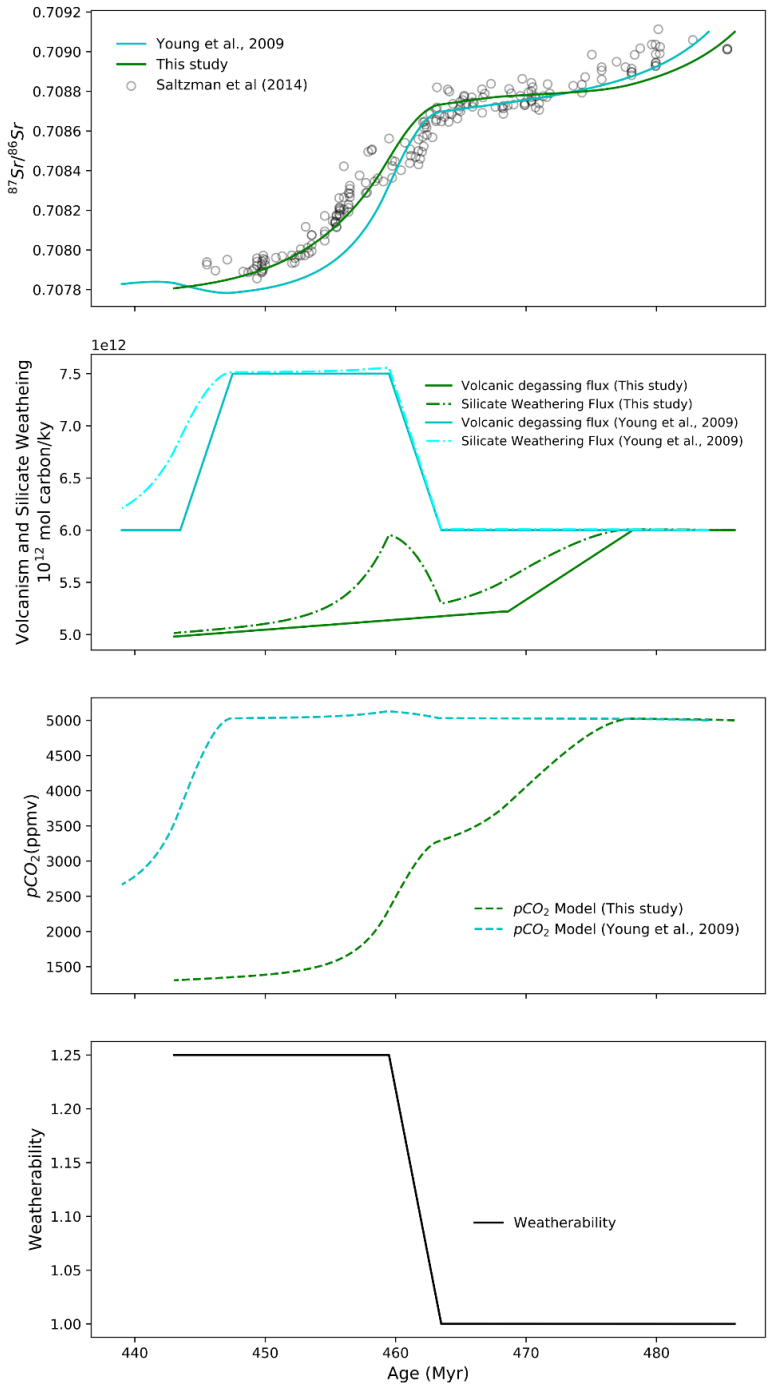


Fig. S1. Comparison of $^{87}Sr/^{86}Sr$ and $pCO_2$ mass balance model results in the original publication (Young et al., 2009) and with our updated degassing parameter based on Cocks and Torsvik (in press). The model scenario we present has a smaller increase in silicate weathering than the original model because the silicate weathering sink flux varies partly as a function of $pCO_2$ (higher $pCO_2$, more silicate weathering). The degassing parameter of the original model was primarily an arbitrary tuneable parameter that was loosely based on widespread bentonite deposition (Young et al., 2009). The weatherability curve shown here applies to both versions of the model.

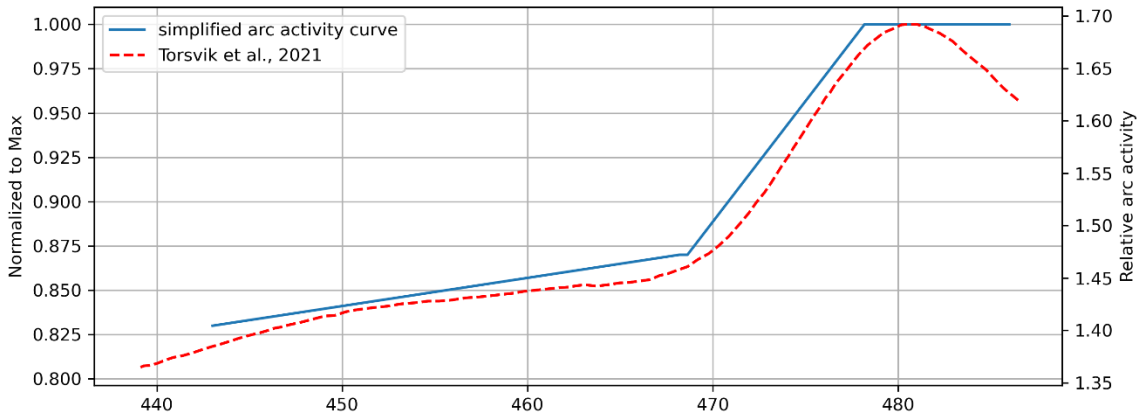


Fig. S2 Relative arc activity curve from Torsvik et al. (2021; see also Marcilly et al., 2021; Cocks and Torsvik, in press) (red dashed line) and the simplified degassing curve used in our $pCO_2$ model (blue solid line). See Supplementary Text for formulation of degassing rate from relative arc activity.

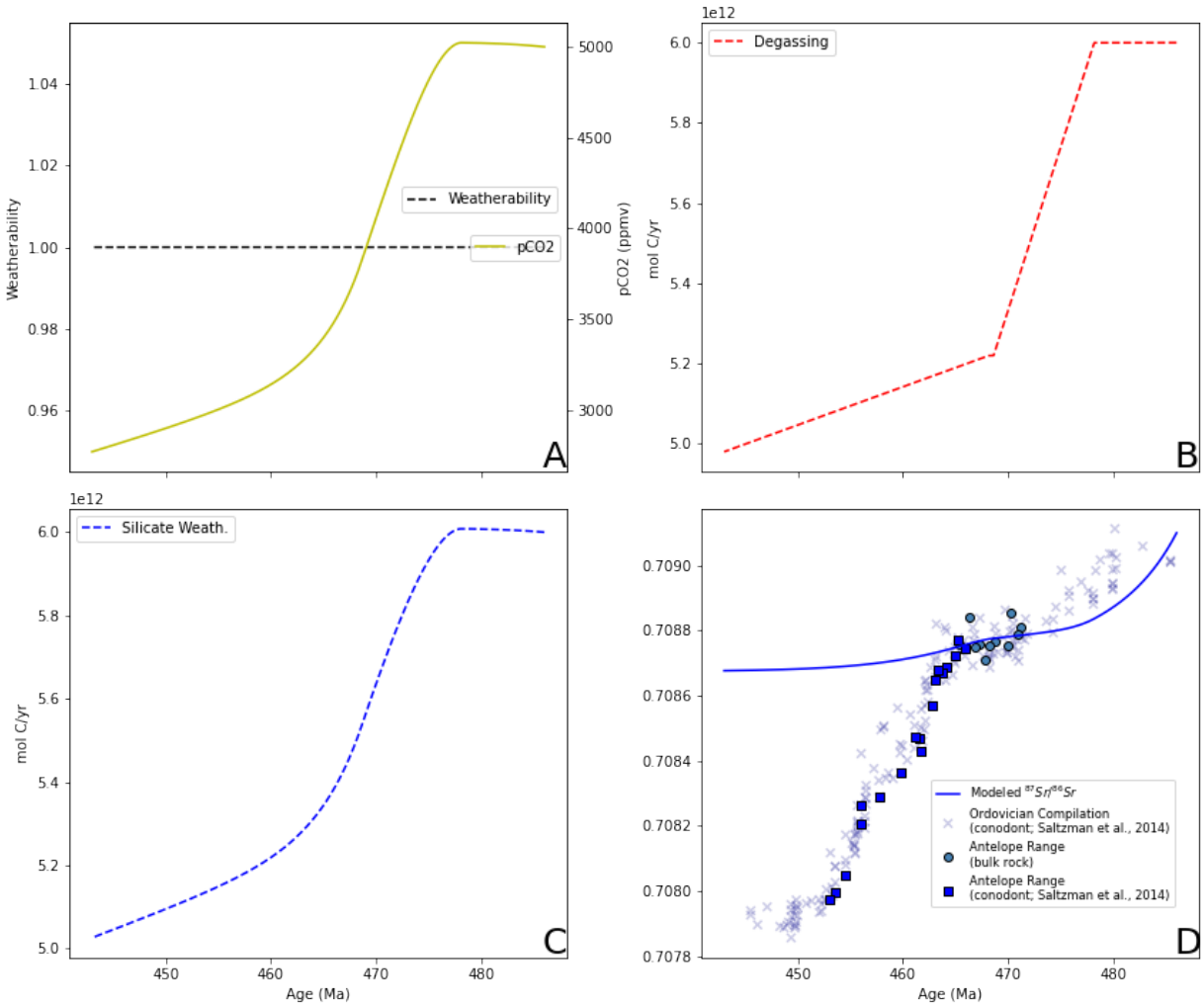


Fig. S3. Results of $^{87}Sr/^{86}Sr$ and $pCO_2$ mass balance model scenario with constant weatherability. (**A**) Weatherability and $pCO_2$ results. (**B**) Degassing parameter based on arc activity reconstruction in Fig. S1. (**C**) $CO_2$ sink fluxes from organic matter (OM) burial and silicate weathering. Decreased fluxes throughout the model run are caused by decreased degassing. (**D**) $^{87}Sr/^{86}Sr$ model output for given weatherability and degassing parameters that poorly represents compiled $^{87}Sr/^{86}Sr$ measurements (Fig. 3B in main text).

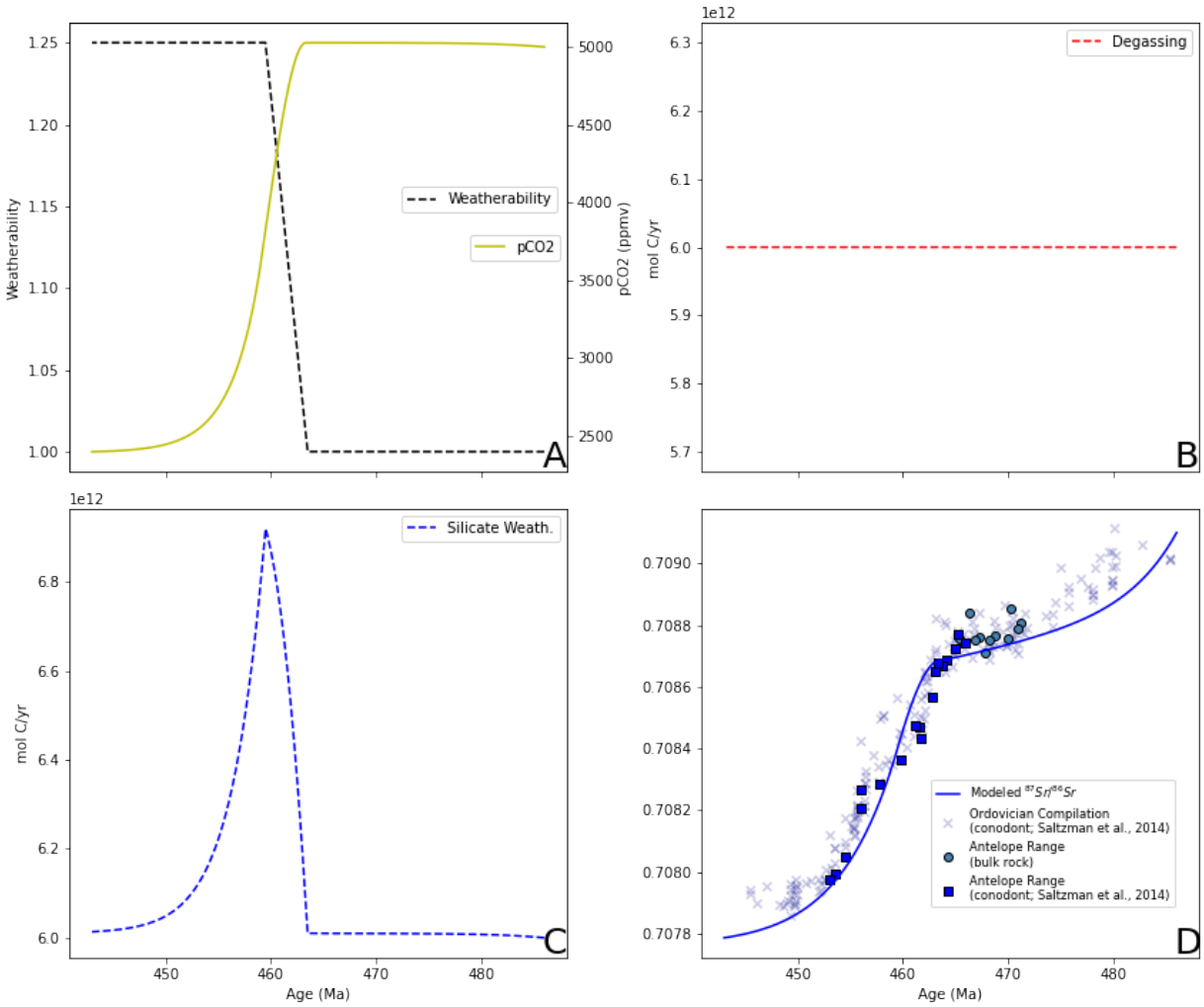


Fig. S4. Results of $^{87}Sr/^{86}Sr$ and $pCO_2$ mass balance model scenario with constant volcanic degassing flux. (**A**) Weatherability and $pCO_2$ results. (**B**) Degassing parameter. (**C**) $CO_2$ sink fluxes from organic matter (OM) burial and silicate weathering. (**D**) $^{87}Sr/^{86}Sr$ model output for given weatherability and degassing parameters that closely models compiled $^{87}Sr/^{86}Sr$ measurements (Fig. 3B in main text).

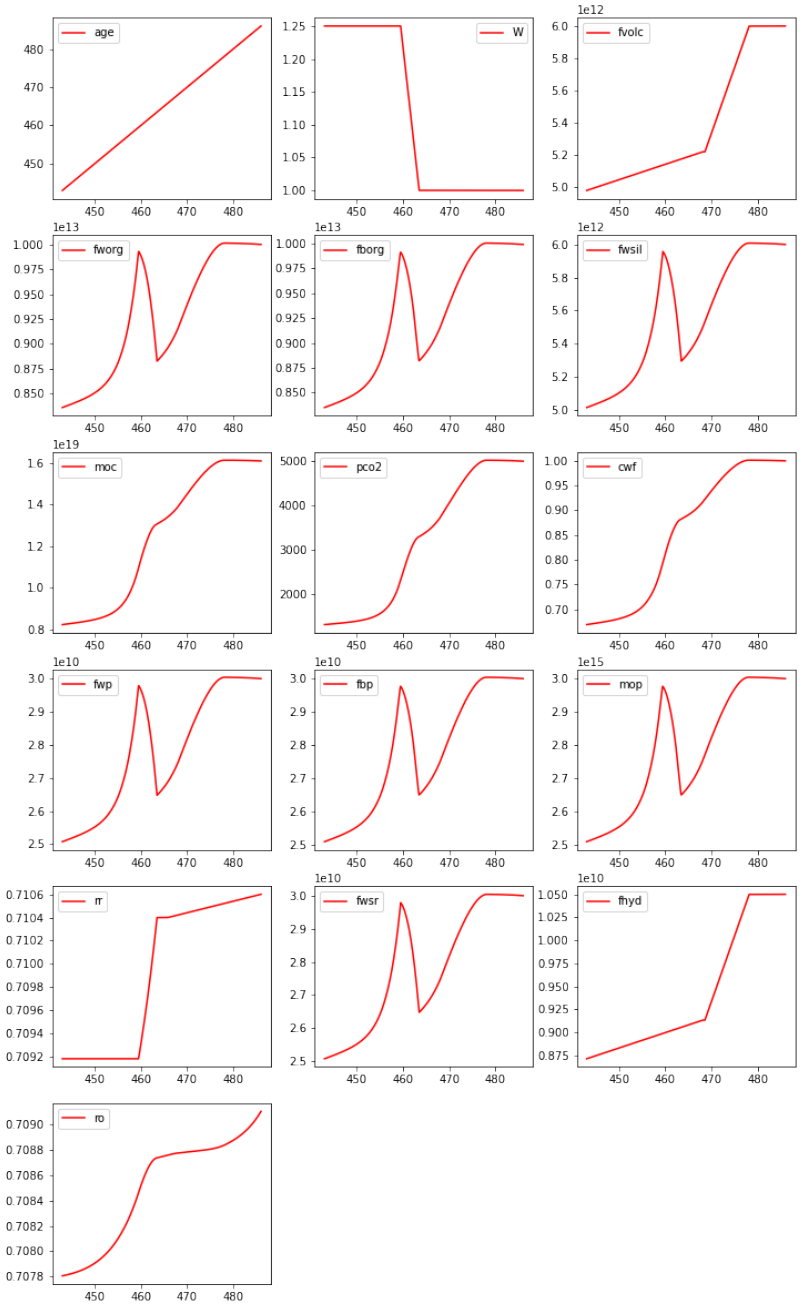


Fig S5. Results of all parameters in our standard isotope mass balance and carbon cycle model. Meaning of symbols with units are the following: W = weatherability [unitless], fvolc = $CO_2$ release from volcanic degassing [$10^{12}$ mol C/yr], fworg = $CO_2$ release from weathering or organic matter [$10^{13}$ mol C/yr], fborg = $CO_2$ captured by organic matter burial [$10^{13}$ mol C/yr], fwsil = $CO_2$ captured by silicate weathering [$10^{12}$ mol C/yr], moc = total inorganic carbon in ocean-atmosphere system [$10^{19}$ mol C], $pCO_2$ = atmospheric $CO_2$ concentration (ppmv), cwf = climate weathering factor [unitless], fwp = flux of phosphate to the oceans [$10^{10}$ mol P/yr], fbp = outflux of phosphate from oceans due to burial [$10^{10}$ mol P/yr], mop = total phosphate in the ocean-atmosphere system [$10^{15}$ mol P], rr = $^{87}Sr/^{86}Sr$ of the riverine flux [unitless], fwsr = flux of Sr to the oceans [$10^{10}$ mol Sr/yr], fhyd = hydrothermal fraction of volcanism, ro = $^{87}Sr/^{86}Sr$ of seawater [unitless]


Fig. S6. Satellite image of Hill 8308 in the Antelope Range of central Nevada (Google Earth ver. 7.3.3.7786) with 2x vertical exaggeration and stratigraphy overlaid. Yellow line shows approximate sampling path. Stretches of sampling path marked with "X"s traverse along strike between outcrops and did not involve any sampling. Note the scale bar at bottom-left.

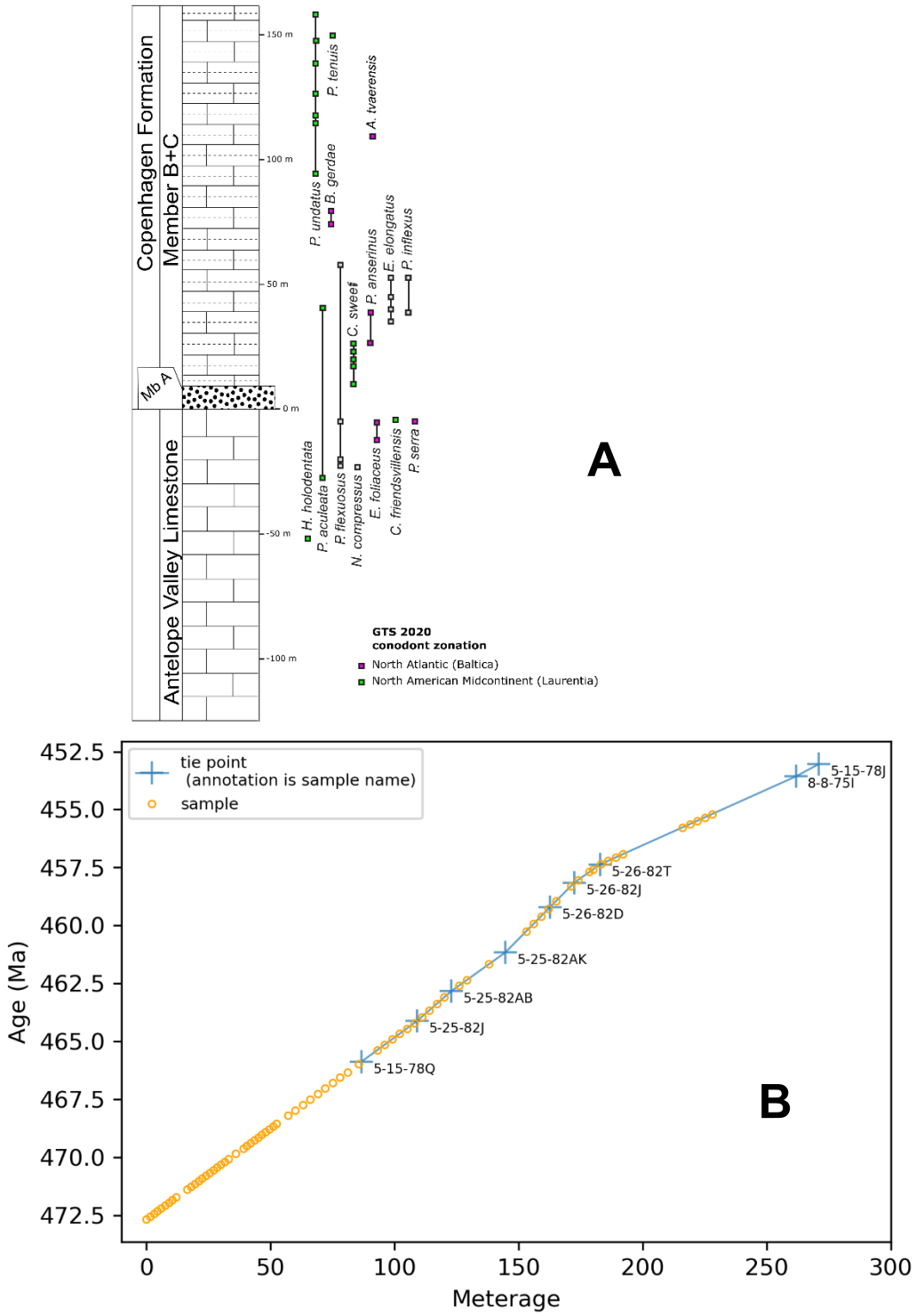


Fig. S7. (A) Occurrences of index conodont taxa in the Hill 8308 section of the Antelope Range, Nevada used in the Geologic Timescale (GTS) 2020 framework (Goldman et al., 2020) modified from Saltzman et al. (2014). (B) An age-depth plot of the age framework used to plot data in Fig. 2. Sample tie points were assigned ages in Saltzman et al. (2014) (converted to GTS 2020) and Edwards et al. (2021).

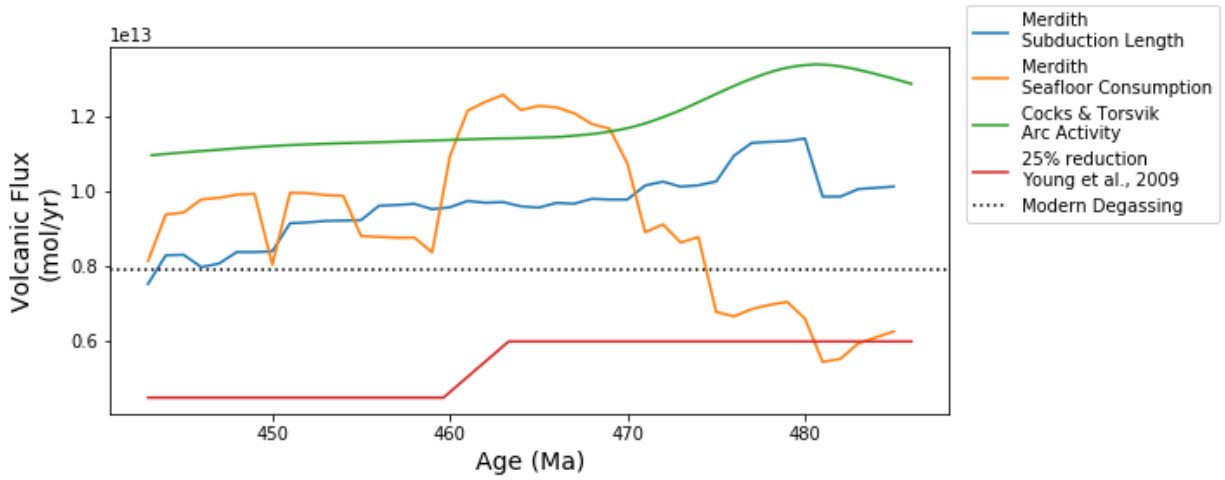


Fig. S8. Comparison of Ordovician volcanic degassing estimates using a variety of relative tectonic activity reconstructions from geodynamic datasets (Young et al., 2009; Merdith et al., 2021; Cocks and Torsvik, in press). The value for modern degassing shown here is from GEOCARBSULF (Berner, 1991). Degassing values here are not scaled to the magnitude of silicate weathering as they are in our model. See Supplementary Text for derivation of degassing parameter from tectonic activity reconstructions.

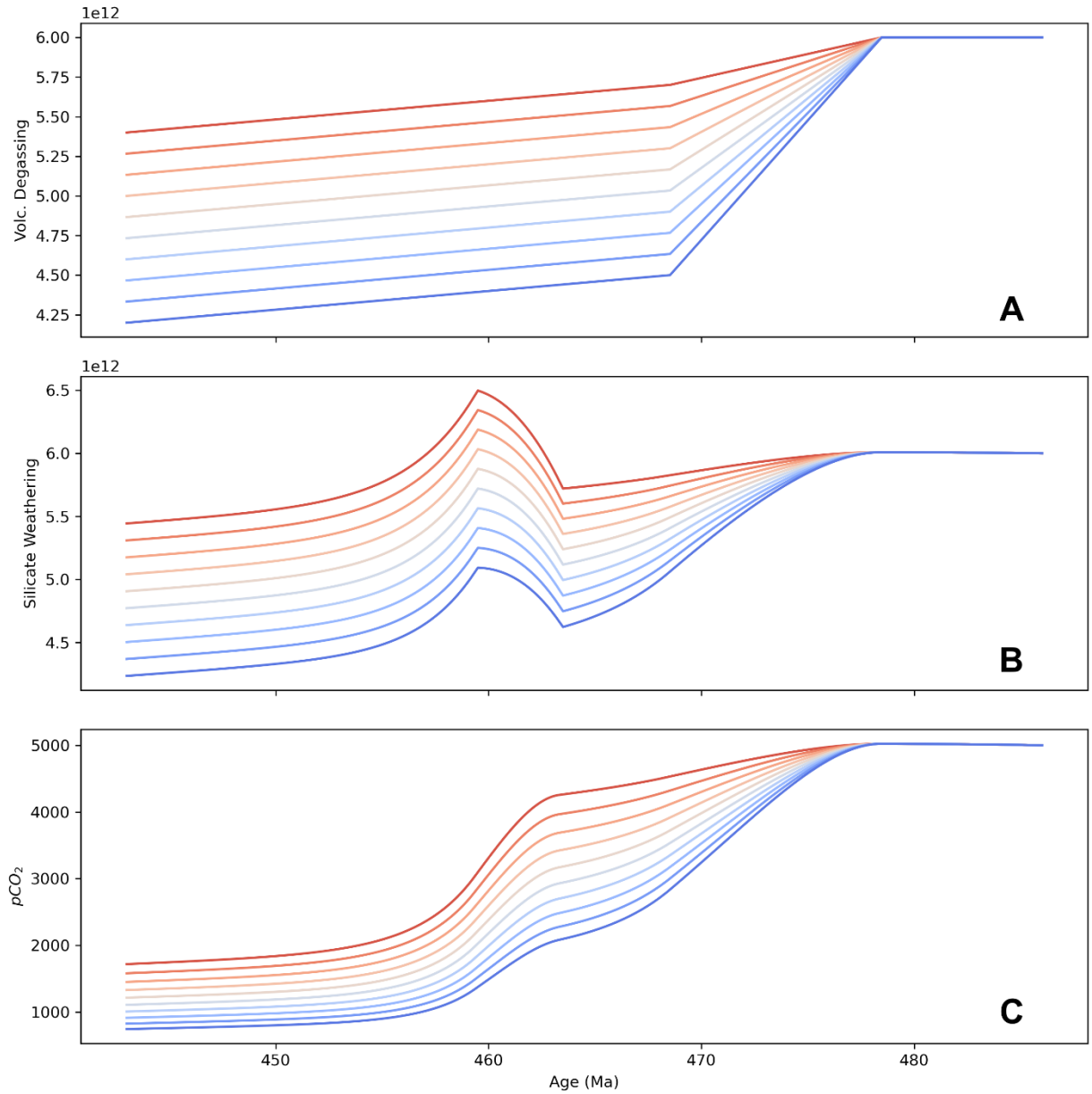


Fig. S9. Sensitivity analysis of volcanic degassing parameter (**A**) and its effect on silicate weathering rate (**B**) and $pCO_2$ (**C**). The degassing parameter used in our model terminates at 4.7 x $10^{12}$ mol C/yr (Fig. 3A in main text). Warmer colors indicate higher degassing rates and therefore higher $pCO_2$ and silicate weathering rates.

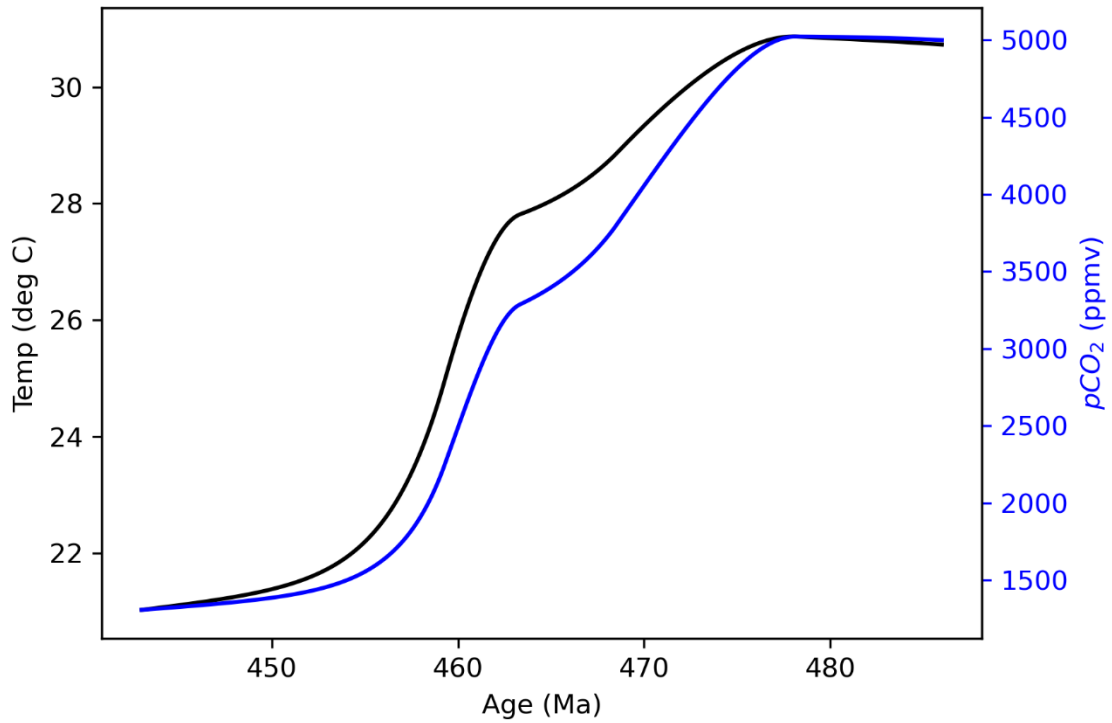


Fig. S10. Modeled paleotemperature (black line) in comparison to our modeled $pCO_2$ record (blue line, also shown in Fig. 3A). See section 4 above for discussion.

## References


Abbott, A.N., Haley, B.A., and McManus, J., 2016, The impact of sedimentary coatings on the diagenetic Nd flux: Earth and Planetary Science Letters, v. 449, p. 217–227, doi:10.1016/j.epsl.2016.06.001.

Abbott, A.N., Löhr, S.C., Payne, A., Kumar, H., and Du, J., 2021, Widespread lithogenic control of marine authigenic neodymium isotope records? Implications for paleoceanographic reconstructions: Geochimica et Cosmochimica Acta, p. S0016703721006761, doi:10.1016/j.gca.2021.11.021.

Andersen, C.B., and Samson, S.D., 1995, Temporal changes in Nd isotopic composition of sedimentary rocks in the Sevier and Taconic foreland basins: Increasing influence of juvenile sources: Geology, v. 23, p. 983, doi:10.1130/0091-7613(1995)023<0983:TCINIC>2.3.CO;2.

Banner, J.L., Hanson, G.N., and Meyers, W.J., 1988, Rare earth element and Nd isotopic variations in regionally extensive dolomites from the Burlington-Keokuk formation (Mississippian): Implications for REE mobility during carboante diagenesis: Journal of Sedimentary Petrology, v. 58, p. 415–432.

Berner, R.A., 1991, A model for atmospheric CO 2 over Phanerozoic time: American Journal of Science, v. 291, p. 339–376, doi:10.2475/ajs.291.4.339.

Berner, R.A., 1994, GEOCARB II: a revised model of atmospheric $CO_2$ over Phanerozoic time: American Journal of Science, v. 294, p. 56–91, doi:10.2475/ajs.294.1.56.

Berner, R.A., 2006, GEOCARBSULF: A combined model for Phanerozoic atmospheric O2 and CO2: Geochimica et Cosmochimica Acta, v. 70, p. 5653–5664, doi:10.1016/j.gca.2005.11.032.

Berner, R.A., and Kothavala, Z., 2001, GEOCARB III: A revised model of atmospheric CO2 over Phanerozoic time: American Journal of Science, v. 301, p. 182–204, doi:10.2475/ajs.301.2.182.

Cocks, L.R.M., and Torsvik, T.H., in press, Ordovician palaeogeography and climate change: Gondwana Research, doi:10.1016/j.gr.2020.09.008.

DePaolo, D.J., and Wasserburg, G.J., 1976, Nd isotopic variations and petrogenetic models: Geophysical Research Letters, v. 3, p. 249–252, doi:10.1029/GL003i005p00249.

Edwards, C.T., Jones, C.M., Quinton, P.C., and Fike, D.A., 2021, Oxygen isotope ($\delta^{18}O$) trends measured from Ordovician conodont apatite using Secondary Ion Mass Spectrometry (SIMS): implications for paleo-thermometry studies: GSA Bulletin, doi:https://doi.org/10.1130/B35891.1.

Edwards, C.T., Saltzman, M.R., Leslie, S.A., Bergström, S.M., Sedlacek, A.R.C., Howard, A., Bauer, J.A., Sweet, W.C., and Young, S.A., 2015, Strontium isotope ( $^{87}Sr/^{86}Sr$) stratigraphy of Ordovician bulk carbonate: Implications for preservation of primary

seawater values: Geological Society of America Bulletin, v. 127, p. 1275–1289, doi:10.1130/B31149.1.

Ethington, R.L., 1969, Conodonts of the Copenhagen Formation (Middle Ordovician) in Central Nevada: Journal of Paleontology, v. 43, p. 440–484.

Fanton, K.C., Holmden, C., Nowlan, G.S., and Haidl, F.M., 2002, $^{143}Nd/^{144}Nd$ and Sm/Nd stratigraphy of Upper Ordovician epeiric sea carbonates: Geochimica et Cosmochimica Acta, v. 66, p. 241–255, doi:10.1016/S0016-7037(01)00773-6.

Foland, K.A., and Allen, J.C., 1991, Magma sources for Mesozoic anorogenic granites of the White Mountain magma series, New England, USA: Contributions to Mineralogy and Petrology, v. 109, p. 195–211, doi:10.1007/BF00306479.

Garver, J.I., Royce, P.R., and Smick, T.A., 1996, Chromium and nickel in shale of the Taconic foreland; a case study for the provenance of fine-grained sediments with an ultramafic source: Journal of Sedimentary Research, v. 66, p. 100–106, doi:10.1306/D42682C5-2B26-11D7-8648000102C1865D.

Gehrels, G., and Pecha, M., 2014, Detrital zircon U-Pb geochronology and Hf isotope geochemistry of Paleozoic and Triassic passive margin strata of western North America: Geosphere, v. 10, p. 49–65.

Goldberg, S.L., Present, T.M., Finnegan, S., and Bergmann, K.D., 2021, A high-resolution record of early Paleozoic climate: Proceedings of the National Academy of Sciences, v. 118, p. e2013083118, doi:10.1073/pnas.2013083118.

Goldman, D., Sadler, P.M., and Leslie, S.A., 2020, The Ordovician Period, *in* Geologic Time Scale 2020, v. 2, p. 631–694.

Grossman, E.L., and Joachimski, M.M., 2020, Oxygen Isotope Stratigraphy, *in* Geologic Time Scale 2020, Elsevier, p. 279–307, doi:10.1016/B978-0-12-824360-2.00010-3.

Harris, A.G., Ethington, R.L., and Ross, R., 1979, Aspects of Middle and Upper Ordovician Conodont Biostratigraphy of Carbonate Facies in Nevada and Southeast California and Comparison with Some Appalachian Successions: , p. 38.

Hatcher, R.D., 2010, The Appalachian orogen: A brief summary, *in* From Rodinia to Pangea: The Lithotectonic Record of the Appalachian Region, Geological Society of America, doi:10.1130/2010.1206(01).

Hiscott, R.N., 1984, Ophiolitic source rocks for Taconic-age flysch: Trace-element evidence: GSA Bulletin, v. 95, p. 1261–1267, doi:10.1130/0016-7606(1984)95<1261:OSRFTF>2.0.CO;2.

Holmden, C., Creaser, R.A., Muehlenbachs, K., Leslie, S.A., and Bergström, S.M., 1998, Isotopic evidence for geochemical decoupling between ancient epeiric seas and bordering

oceans: Implications for secular curves: Geology, v. 26, p. 567, doi:10.1130/0091-7613(1998)026<0567:IEFGDB>2.3.CO;2.

Karabinos, P., Macdonald, F.A., and Crowley, J.L., 2017, Bridging the gap between the foreland and hinterland I: Geochronology and plate tectonic geometry of Ordovician magmatism and terrane accretion on the Laurentian margin of New England: American Journal of Science, v. 317, p. 515–554, doi:10.2475/05.2017.01.

Keto, L.S., and Jacobsen, S.B., 1987, Nd and Sr isotopic variations of Early Paleozoic oceans: Earth and Planetary Science Letters, v. 84, p. 27–41, doi:10.1016/0012-821X(87)90173-7.

Krogh, T.E., and Hurley, P.M., 1968, Strontium isotope variation and whole-rock isochron studies, Grenville Province of Ontario: Journal of Geophysical Research, v. 73, p. 7107–7125, doi:10.1029/JB073i022p07107.

Lee, C.-T.A., Thurner, S., Paterson, S., and Cao, W., 2015, The rise and fall of continental arcs: Interplays between magmatism, uplift, weathering, and climate: Earth and Planetary Science Letters, v. 425, p. 105–119, doi:10.1016/j.epsl.2015.05.045.

Lenton, T.M., Daines, S.J., and Mills, B.J.W., 2018, COPSE reloaded: An improved model of biogeochemical cycling over Phanerozoic time: Earth-Science Reviews, v. 178, p. 1–28, doi:10.1016/j.earscirev.2017.12.004.

Marcilly, C.M., Torsvik, T.H., Domeier, M., and Royer, D.L., 2021, New paleogeographic and degassing parameters for long-term carbon cycle models: Gondwana Research, v. 97, p. 176–203, doi:10.1016/j.gr.2021.05.016.

McKenzie, N.R., Horton, B.K., Loomis, S.E., Stockli, D.F., Planavsky, N.J., and Lee, C.-T.A., 2016, Continental arc volcanism as the principal driver of icehouse-greenhouse variability: Science, v. 352, p. 444–447, doi:10.1126/science.aad5787.

McKenzie, N.R., Hughes, N.C., Gill, B.C., and Myrow, P.M., 2014, Plate tectonic influences on Neoproterozoic–early Paleozoic climate and animal evolution: Geology, v. 42, p. 127–130, doi:10.1130/G34962.1.

Merdith, A.S. et al., 2021, Extending full-plate tectonic models into deep time: Linking the Neoproterozoic and the Phanerozoic: Earth-Science Reviews, v. 214, p. 103477, doi:10.1016/j.earscirev.2020.103477.

Montañez, I.P., Banner, J.L., Osleger, D.A., Borg, L.E., and Bosserman, P.J., 1996, Integrated Sr isotope variations and sea-level history of Middle to Upper Cambrian platform carbonates: Implications for the evolution of Cambrian seawater 87Sr/86Sr: Geology, v. 24, p. 917–920, doi:10.1130/0091-7613(1996)024<0917:ISIVAS>2.3.CO;2.

Pohl, A., Donnadieu, Y., Le Hir, G., Ladant, J., Dumas, C., Alvarez-Solas, J., and Vandenbroucke, T.R.A., 2016, Glacial onset predated Late Ordovician climate cooling: Paleoceanography, v. 31, p. 800–821, doi:10.1002/2016PA002928.

Pope, M.C., and Steffen, J.B., 2003, Widespread, prolonged late Middle to Late Ordovician upwelling in North America: A proxy record of glaciation? Geology, v. 31, p. 63, doi:10.1130/0091-7613(2003)031<0063:WPLMTL>2.0.CO;2.

Rasmussen, C.M.Ø. et al., 2016, Onset of main Phanerozoic marine radiation sparked by emerging Mid Ordovician icehouse: Scientific Reports, v. 6, doi:10.1038/srep18884.

Ross, R.J., 1976, Ordovician sedimentation in the Western United States: Rocky Mountain Association of Geologists, http://archives.datapages.com/data/rmag/GeolCordHing76/ross.pdf (accessed November 2019).

Saltzman, M.R., Edwards, C.T., Leslie, S.A., Dwyer, G.S., Bauer, J.A., Repetski, J.E., Harris, A.G., and Bergström, S.M., 2014, Calibration of a conodont apatite-based Ordovician $^{87}Sr/^{86}Sr$ curve to biostratigraphy and geochronology: Implications for stratigraphic resolution: Geological Society of America Bulletin, v. 126, p. 1551–1568, doi:10.1130/B31038.1.

Saltzman, M.R., and Young, S.A., 2005, Long-lived glaciation in the Late Ordovician? Isotopic and sequence-stratigraphic evidence from western Laurentia: Geology, v. 33, p. 109, doi:10.1130/G21219.1.

Spencer, A.W., 1984, The Conodont Biostratigraphy and Paleoecology Across the Whiterockian-Mohawkian Series Boundary in the Copenhagen Formation, Antelope Range, Nye County, Nevada: Colorado School of Mines, 56 p.

Swanson-Hysell, N.L., and Macdonald, F.A., 2017, Tropical weathering of the Taconic orogeny as a driver for Ordovician cooling: Geology, v. 45, p. 719–722, doi:10.1130/G38985.1.

Sweet, W.C., Ethington, R.L., and Harris, A.G., 2005, A conodont-based standard reference section in central Nevada for the lower Middle Ordovician Whiterockian Series: Bulletins of American Paleontology, v. 2005, p. 35–48.

Theiling, B.P., Elrick, M., and Asmerom, Y., 2017, Constraining the timing and provenance of trans-Laurentian transport using Nd and Sm isotopes from Silurian and Devonian marine carbonates: Palaeogeography, Palaeoclimatology, Palaeoecology, v. 466, p. 392–405, doi:10.1016/j.palaeo.2016.09.012.

Torsvik, T.H., Svensen, H.H., Steinberger, B., Royer, D.L., Jerram, D.A., Jones, M.T., and Domeier, M., 2021, Connecting the Deep Earth and the Atmosphere, *in* Mantle Convection and Surface Expressions, American Geophysical Union (AGU), p. 413–453, doi:10.1002/9781119528609.ch16.

Young, S.A., Saltzman, M.R., Foland, K.A., Linder, J.S., and Kump, L.R., 2009, A major drop in seawater $^{87}Sr/^{86}Sr$ during the Middle Ordovician (Darriwilian): Links to volcanism and climate? Geology, v. 37, p. 951–954, doi:10.1130/G30152A.1.

Zelinka, M.D., Myers, T.A., McCoy, D.T., Po-Chedley, S., Caldwell, P.M., Ceppi, P., Klein, S.A., and Taylor, K.E., 2020, Causes of Higher Climate Sensitivity in CMIP6 Models: Geophysical Research Letters, v. 47, p. e2019GL085782, doi:10.1029/2019GL085782.